crystals

MDPI

*Article*

# Synthesis of O,F Co-Modified g-$C_3N_4$ for Photocatalytic $H_2$ Evolution Activity Improvement and Corrosion Protection

**Shiyu Zhou [1,2,*], Pei Li [1,2], Chunbo Zhang [1,2], Yang Wang [1,2], Jingting Hu [1,2] and Ruokun Jia [3,*]**

[1] Jilin Province Electric Power Research Institute, Changchun 130021, China; lipei515@126.com (P.L.); zcb1221@163.com (C.Z.); 13578741456@139.com (Y.W.); 15843072993@163.com (J.H.)
[2] State Grid Jilin Electric Power Research Institute, Changchun 130021, China
[3] College of Chemical Engineering, Northeast Electric Power University, Jilin City 132012, China
* Correspondence: fiona1207@163.com (S.Z.); jiaruokun@163.com (R.J.)

**Abstract:** Herein, we report the rational synthesis of porous g-$C_3N_4$ co-modified with oxygen (O) and fluorine (F) for the first time. Incorporating colloidal $SiO_2$ during thermal polymerization introduces lattice oxygen, forming C–O bonds, while post-treatment with $NH_4{\cdot}HF_2$ establishes C–F bonds. The dual incorporation of O and F elements extends visible light absorption and effectively promotes the separation and transport of photoexcited charge carriers. Consequently, the co-modified g-$C_3N_4$ (O,F-g-$C_3N_4$) achieves a 13.2-fold increase in $H_2$ evolution rate compared to pristine g-$C_3N_4$. This synthesized O,F-g-$C_3N_4$ is then dispersed in waterborne polyurethane (WPU) to create an anti-corrosive coating for Q235 carbon steel substrates. Water resistance, mechanical property, and electrochemical characterization analyses reveal that the O,F-g-$C_3N_4$/WPU composite coating exhibits remarkable corrosion resistance with a high protection efficiency of 90.23%. This work offers a straightforward approach for developing highly efficient g-$C_3N_4$-based photocatalysts and corrosion-resistant coatings.

**Keywords:** g-$C_3N_4$; O,F co-modification; photocatalytic $H_2$ evolution; anti-corrosion

check for updates

**Citation:** Zhou, S.; Li, P.; Zhang, C.; Wang, Y.; Hu, J.; Jia, R. Synthesis of O,F Co-Modified g-$C_3N_4$ for Photocatalytic $H_2$ Evolution Activity Improvement and Corrosion Protection. *Crystals* **2024**, *14*, 1063. https://doi.org/10.3390/cryst14121063

Academic Editor: Nabeen K Shrestha

Received: 17 November 2024
Revised: 29 November 2024
Accepted: 2 December 2024
Published: 9 December 2024

**Copyright:** © 2024 by the authors. Licensee MDPI, Basel, Switzerland. This article is an open access article distributed under the terms and conditions of the Creative Commons Attribution (CC BY) license (https://creativecommons.org/licenses/by/4.0/).

## 1. Introduction

Graphitic carbon nitride (g-$C_3N_4$) is a promising metal-free semiconductor, valued for its visible-light responsiveness, chemical and thermal stability, non-toxicity, ease of synthesis, and low cost [1]. It has become a preferred material for photocatalytic applications in renewable energy production and environmental pollution remediation, due to its strong thermodynamic driving force and moderate dispersibility in water [2]. Hydrogen, as a secondary energy source, is regarded as a viable alternative to traditional fossil fuels, with potential to address global energy and environmental challenges [3,4]. Since the seminal 1972 report by Fujishima and Honda on photoelectrochemical water splitting using a Pt-$TiO_2$ electrode, photocatalytic $H_2$ production via semiconductor technology has garnered substantial interest [5]. Significant efforts have thus been directed toward developing high-efficiency, g-$C_3N_4$-based photocatalysts with robust $H_2$ evolution performance to satisfy industrial demands [6]. However, the low specific surface area of pristine g-$C_3N_4$ restricts the availability of active catalytic sites, thereby limiting photocatalytic activity enhancement [7–9]. Additionally, the widespread use of g-$C_3N_4$ is hindered by the low separation efficiency of photo-induced electron–hole pairs, as the π-deficient conjugated structure results in high exciton recombination energy and transport resistance for photoexcited carriers [10,11].

Template methods have been explored to enhance the surface area and photocatalytic efficiency of g-$C_3N_4$ [12–14]. Researchers commonly use hard templates, such as $SiO_2$, mesoporous silica, $CaCO_3$ and anodic aluminum oxide (AAO), to develop g-$C_3N_4$-based photocatalysts. Removing these templates yields a porous architecture with increased

surface area, which efficiently facilitates the mass transfer of reactant molecules and significantly boosts $H_2$ evolution from water [15–18]. However, the template strategy alone does not address the material's poor electronic properties. As a π-deficient conjugated polymer composed of carbon and nitrogen atoms, bare g-$C_3N_4$ suffers from strong electron localization, leading to low carrier density, reduced mobility, and limited photoelectric conversion efficiency [19].

To further enhance photocatalytic $H_2$ production, modifying the π-deficient conjugated system is crucial. Studies have shown that incorporating heteroatoms into the g-$C_3N_4$ framework can optimize local electron distribution and adjust the electronic band structure, thereby facilitating photoelectric conversion [20]. Given its heptazine-based polymer structure, incorporating elements with higher electronegativity than C and N can enhance electron density and increase carrier mobility in g-$C_3N_4$. For example, Lan et al. demonstrated that modifications with Br, F, I, or O significantly improved the photoelectrical properties and photocatalytic performance of g-$C_3N_4$ [21–24]. However, single-component modification has a limited effect on tailoring the electronic structure, making further enhancement of activity challenging. Therefore, we propose that preparing porous g-$C_3N_4$ modified with dual elements is a rational strategy to further boost photocatalytic $H_2$ generation.

Beyond photocatalytic $H_2$ evolution, the economic and societal impacts of corrosion on steel structures are profound, posing a significant challenge within materials science and engineering due to the immense costs and structural risks involved [25]. Developing efficient corrosion-resistant coatings that can prevent or substantially mitigate steel corrosion is therefore a critical area of focus. Recently, g-$C_3N_4$ has emerged as a promising material for anti-corrosion coatings. For instance, Zhang et al. reported that tannic acid-modified g-$C_3N_4$ nanosheets combined with polydimethylsiloxane demonstrated exceptional corrosion resistance [26]. Samadianfard et al. developed a sol–gel nanocomposite incorporating inhibitor-stabilized g-$C_3N_4$ nanoplates to protect magnesium alloys from corrosion [27]. Additionally, Hasanzadeh et al. designed ZIF-67 metal–organic framework-decorated g-$C_3N_4$ nanosheets for epoxy-based anti-corrosion coatings [28]. These studies illustrate that g-$C_3N_4$-based materials not only facilitate photocatalytic $H_2$ production but also exhibit effective corrosion resistance, making them highly suitable for multifunctional anti-corrosion coatings, particularly for advanced protective applications in marine engineering.

In this study, porous g-$C_3N_4$ modified with O and F binary elements was synthesized via in situ thermal polymerization followed by post-treatment with $NH_4{\cdot}HF_2$. The introduction of colloidal $SiO_2$ nanospheres and subsequent $NH_4{\cdot}HF_2$ etching facilitated a porous structure and increased the surface area of the resulting g-$C_3N_4$. Additionally, the use of colloidal $SiO_2$ and extended post-processing time enabled the incorporation of O and F into the heptazine framework, forming C–O and C–F bonds. This porous structure, coupled with dual-element co-modification, synergistically enhanced the photocatalytic $H_2$ evolution. Subsequently, we engineered O,F-g-$C_3N_4$/waterborne polyurethane (WPU) composite coatings to improve corrosion protection for Q235 carbon steel. Electrochemical characterizations demonstrated the superior corrosion resistance and protection efficiency of O,F-g-$C_3N_4$/WPU composite coatings compared to unmodified WPU coatings.

## 2. Experimental Section

### *2.1. Chemicals and Materials*

Colloidal $SiO_2$ nanospheres (40 wt.% suspension in $H_2O$, ~50 nm (DLS)) were purchased from Sigma-Aldrich Company. Dicyandiamide ($C_2H_4N_4$, DCDA), chloroplatinic acid ($H_2PtCl_6{\cdot}6H_2O$), triethanolamine (TEOA), and sodium sulfate ($Na_2SO_4$) were purchased from Beijing Reagent Co., Ltd., Beijing, China. Ammonium bifluoride ($NH_4{\cdot}HF_2$) and sodium chloride (NaCl) were purchased from Shanghai Macklin Biochemical Technology Corp., Ltd., Shanghai, China. Water-borne polyurethane (WPU) was purchased from Shenzhen Jitian chemical Co., Ltd., Shenzhen, China. All the reagents in this research were analytical-grade and used without further purification. Indium tin oxide (ITO) glass

was purchased from Kaisheng Technology Co., Ltd., Changsha, China. Deionized water (Millipore, 18.2 MΩ·cm) was used throughout all the experiments.

### *2.2. Sample Preparation*

#### 2.2.1. Synthesis of Pristine g-$C_3N_4$

The bulk g-$C_3N_4$ was prepared by direct thermal polymerization of DCDA. Typically, 1 g of DCDA was placed into a crucible, which was transferred into a muffle furnace for polymerization at 520 °C for 2 h with a heating rate of 5 °C·min$^{-1}$.

#### 2.2.2. Synthesis of O,F-g-$C_3N_4$

For the synthesis of the g-$C_3N_4$/$SiO_2$ composite, a specified amount of colloidal $SiO_2$, 1 g of DCDA, and 4 mL of $H_2O$ were mixed at room temperature under magnetic stirring for 2 h. The mixture was then transferred to a porcelain crucible and placed in a vacuum oven at 45 °C until completely dried. The resulting white powder was ground and subsequently calcined in a muffle furnace at 520 °C for 2 h with a heating rate of 10 °C·min$^{-1}$. A heating rate of 10 °C·min$^{-1}$ was selected to reduce the reaction preparation time. After natural cooling to room temperature, the light yellow powder was thoroughly ground in an agate mortar. This powder was then dispersed in 100 mL of a supersaturated $NH_4 \cdot HF_2$ solution and stirred for 24 h. The precipitate was washed with $H_2O$ until the pH of the supernatant was neutral. Finally, the resulting brown product was dried and donated as O,F-g-$C_3N_4$.

#### 2.2.3. Synthesis of O,F-g-$C_3N_4$@WPU Composite

The O,F-g-$C_3N_4$@WPU composite was synthesized by a mild ultrasonic procedure. First, a predetermined amount of previously prepared O,F-g-$C_3N_4$ powder was dispersed in 10 g of WPU with magnetic stirring at 350 rpm for 1 h. The mixture was then subjected to ultrasonication at 25 °C for 1.5 h (ultrasonic power: 120 W; ultrasonic frequency: 40 kHz). This process yielded a stable colloidal dispersion without visible precipitation, labeled as O,F-g-$C_3N_4$@WPU. The optimal amount of O,F-g-$C_3N_4$ powder added was determined to be 50 mg.

#### 2.2.4. Preparation of O,F-g-$C_3N_4$@WPU Coating on Q235 Carbon Steel Substrate

The Q235 steel plates were pre-polished with 800#, 1000# and 1200# sheets of sandpaper to get rid of the surface oxide layer and rust. Then, the Q235 steel plates were ultrasonically cleaned in absolute ethanol for 30 min to remove the surface stains and dried at room temperature. The prepared composite coatings were prepared as follows: Firstly, a certain amount of O,F-g-$C_3N_4$@WPU was mixed with a small amount of defoamer by stirring for 10 min, and the mixture was applied to the surface of Q235 carbon steel and cured at room temperature for 12 h.

### *2.3. Characterizations*

The morphology of the colloidal $SiO_2$, bare g-$C_3N_4$ and O,F-g-$C_3N_4$ samples was observed on a Supramol scanning electron microscope (SEM). A total of 5 mg of colloidal $SiO_2$, bare g-$C_3N_4$ and O,F-g-$C_3N_4$ samples was dispersed into 3 mL $H_2O$ and sonicated for 20 min. The obtained dispersion was dropped onto the surface of a silicon wafer and allowed to dry completely in a vacuum-drying oven. Once dried, the sample was transferred to the sampling chamber for morphology observation under an operating voltage of 5 KV. The molecular structure of the samples was characterized by Fourier transform infrared (FTIR) spectra. A total of 2 mg of dried samples was mixed with spectrally pure KBr and pressed into a pellet for infrared spectrum testing using an IRAffinity-1 spectrometer. The crystal structure was characterized by a D/MAX-2200/PC X-ray diffractometer with Cu Kα radiation at a scanning rate of 5 °/min. The powder sample was loaded onto a glass sample stage with a groove measuring 1 × 1 cm to obtain powder X-ray diffraction (XRD) patterns. The chemical state of elements was analyzed on a PHI Quantera II X-ray photoelectron spectrometer using nonmonochromatized Al-Kα radiation. Avantage 5.9931 software was

used for calibration and peak splitting. The specific surface areas and pore size distribution were tested using a Micromeritics ASAP2460 surface area and porosity analyzer. A total of 150 mg of the samples was degassed at 120 °C for 8 h, followed by the collection of the $N_2$ adsorption–desorption isotherm at 77 K. The UV–vis diffuse reflectance spectrum (DRS) was recorded on a Shimadzu UV-2550 spectrometer with $BaSO_4$ as the reference material in the wavelength range of 200–800 nm. A total of 15 mg of samples was sandwiched between two quartz plates and placed on the sample stage. The samples were irradiated with a 365 nm excitation light source to obtain steady-state photoluminescence (PL) emission spectra using a RF-5301PC Spectrofluorophotometer. PL decay curves were collected on a HORIBA Scientific DeltaflexFlex fluorescence lifetime system. The adhesion force measurement was conducted by using a tensile adhesion tester, with a 20 mm spindle and a tensile force increase rate of 0.7 MPa/s. A water absorption test of the coatings was performed according to the national standard H/GT 3344-1985 [29].

### *2.4. Electrochemical Measurements*

Electrochemical tests were carried out on a Chenhua CHI660E electrochemical workstation with a standard triple electrode cell (total volume of 150 mL). For the photoelectrochemical measurements, a gauze platinum, Ag/AgCl (saturated KCl) and FTO glass coated with the O,F-g-$C_3N_4$ photocatalyst were used as the counter electrode, reference electrode and working electrode, respectively. The three electrodes were immersed in an electrolyte solution of $Na_2SO_4$ (0.5 M, 100 mL). A 300 W Xe lamp (PLS-SXE300, Perfect Light) was used as the irradiation light source. The working electrode was illuminated to record the transient photocurrent response in 400 s. Electrochemical impedance spectroscopy (EIS) was performed under a disturbance signal of 5 mV with a frequency range from 0.1 Hz to 100 kHz. For the photocatalytic anti-corrosion resistance test, Q235 carbon steel coated with an O,F-g-$C_3N_4$@WPU membrane was employed as the working electrode. The three electrodes were immersed in an electrolyte solution of NaCl (3.5 wt.%, 100 mL). The EIS spectrum was measured over a frequency range of 0.01–100,000 Hz under an AC amplitude of 5 mV. The polarization curve (Tafel) was measured with a voltage range of −1.0–0.2 V using a saturated calomel electrode (SCE) as the reference electrode [30]. The protection efficiency (η) was calculated as follows:

$$\eta = \frac{i_{corr,0} - i_{corr,i}}{i_{corr,0}} \times 100\%$$

where $i_{corr,0}$ is the corrosion current density of uncoated Q235 carbon steel, and $i_{corr,i}$ is the corrosion current density of Q235 carbon steel after coating.

### *2.5. Photocatalytic Activity Measurements*

The photocatalytic $H_2$ generation tests were performed in a closed quartz reactor. Briefly, 100 mg of the as-prepared photocatalyst powders were dispersed into a 300 mL aqueous solution containing 10 vol% TEOA as a hole sacrificial agent. After 30 min of magnetic stirring, the suspension was aerated by high-purity $N_2$ (99.999%) at a flux of 0.3 L·min$^{-1}$ to remove dissolved $O_2$. $H_2$ evolution was then initiated by using a 300 W Xe lamp irradiation with a cut-off filter ($\lambda \geq 420$ nm). The amount of generated $H_2$ was analyzed by a Fuli GC9790II gas chromatograph equipped with a thermal conductivity detector (TCD) (Shiyanjia Lab: www.shiyanjia.com, accessed on 17 January 2024). The $H_2$ production rate was calculated as follows:

$$R = \frac{V(H_2)}{t \cdot m \cdot V_m}$$

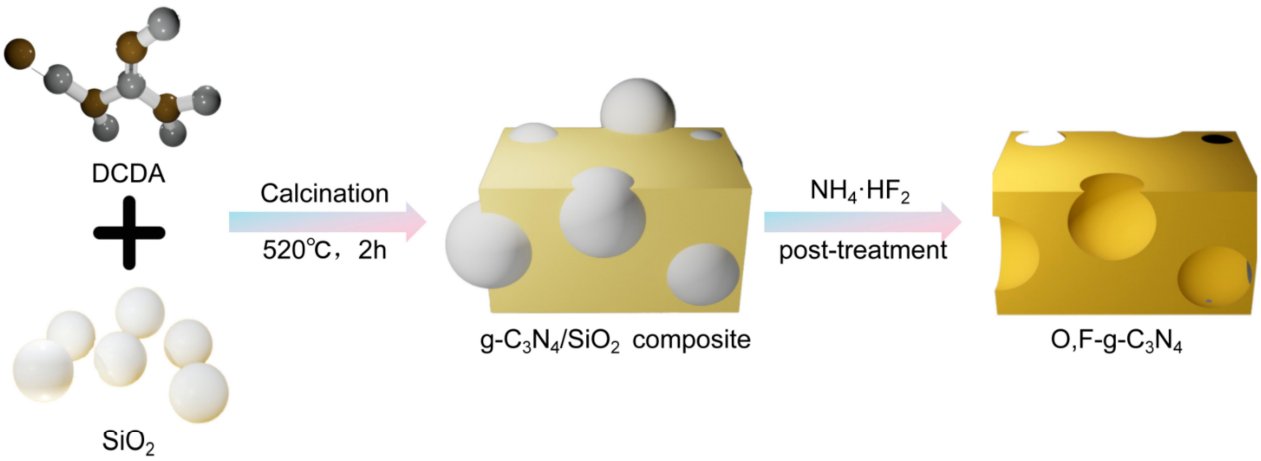
where R is the $H_2$ evolution rate (μmol·g$^{-1}$·h$^{-1}$), $V(H_2)$ is the volume of generated $H_2$ (mL), t is the photocatalytic reaction time (h), m is the weight of the photocatalyst (g), and $V_m$ is the molar volume (under standard conditions, 22.4 L·mol$^{-1}$).

Cyclic $H_2$ production measurements were conducted in a closed quartz reaction vessel containing 100 mg of the dispersed photocatalyst, 10 vol% TEOA and 300 mL of $H_2O$. The system was purged with high-purity $N_2$ (99.999%) for 20 min to remove residual $O_2$. We turned on a light source (300 W) with a cut-off filter ($\lambda \geq 420$ nm) to initiate the photocatalytic reaction and monitor $H_2$ production with a Fuli GC9790II gas chromatograph equipped with a TCD detector. After the reaction had proceeded for 5h, we turned off the light source and recovered the photocatalyst through centrifugation. We washed the recovered photocatalyst with distilled water to remove residual sediments. We repeated the steps above (purge with argon, initiate reaction, monitor hydrogen production) for four cycles to evaluate the reusability of the catalyst.

## 3. Results and Discussion

### *3.1. Morphology and Structure Characterization*

An O and F co-modified g-$C_3N_4$ photocatalyst was synthesized by using colloidal $SiO_2$ as the O source and $NH_4{\cdot}HF_2$ as the F source. In the presence of colloidal $SiO_2$, dicyandiamide undergoes polyaddition and polycondensation processes to produce polymeric g-$C_3N_4$ (as illustrated in Scheme 1). The morphology of the colloidal $SiO_2$, bare g-$C_3N_4$ and O,F-g-$C_3N_4$ samples was observed by scanning electron microscopy. The colloidal $SiO_2$ displayed spherical nanoparticles with an average size of 50–60 nm (Figure 1a). Pristine g-$C_3N_4$ exhibited an irregular block-like structure with stacked layers (Figure 1b). Following $NH_4{\cdot}HF_2$ post-treatment, the surface of g-$C_3N_4$ became rough and developed a porous structure (Figure 1c,d). Nitrogen adsorption–desorption measurements were performed to assess the effect of the $NH_4{\cdot}HF_2$ post-treatment on the porosity of the g-$C_3N_4$ photocatalyst. The pore size values presented in Table S1 were determined from the desorption branch of the isotherm. A typical hysteresis loop of the isotherm indicates the mesoporous characteristics of the prepared samples (Figure 1e), which are consistent with the pore size distribution curve (Figure 1f). With respect to the bare g-$C_3N_4$, the O,F-g-$C_3N_4$ photocatalyst demonstrated increased surface area and pore volume (Table S1), illustrating that the $NH_4{\cdot}HF_2$ post-treatment was favorable to elevate the surface areas and increase exposed active sites, which was beneficial for photocatalytic $H_2$ generation performance improvement.




**Scheme 1.** Preparation procedure illustration for O,F-g-$C_3N_4$ sample.

FTIR spectra and XRD patterns were employed to analyze the molecular and crystalline structures of colloidal $SiO_2$, pristine g-$C_3N_4$ and O,F-g-$C_3N_4$ samples. As shown in Figure 2a, a broad absorption band at 1114 $cm^{-1}$ corresponded to the characteristic Si-O-Si antisymmetric stretching vibration. Additionally, peaks at 471 $cm^{-1}$ and 802 $cm^{-1}$ were attributed to the Si-O bending vibration and the symmetric stretching vibration of the Si-O bond, respectively [25]. The peak at 807 $cm^{-1}$ represented the typical characteristic absorption of the heptazine ring in g-$C_3N_4$, while a series of peaks within the

range of 1200–1700 $cm^{-1}$ were characteristic absorptions of CN heterocycles [31]. The O,F-g-$C_3N_4$ sample exhibited only the characteristic absorptions of g-$C_3N_4$, indicating that the fundamental heptazine framework remained intact.

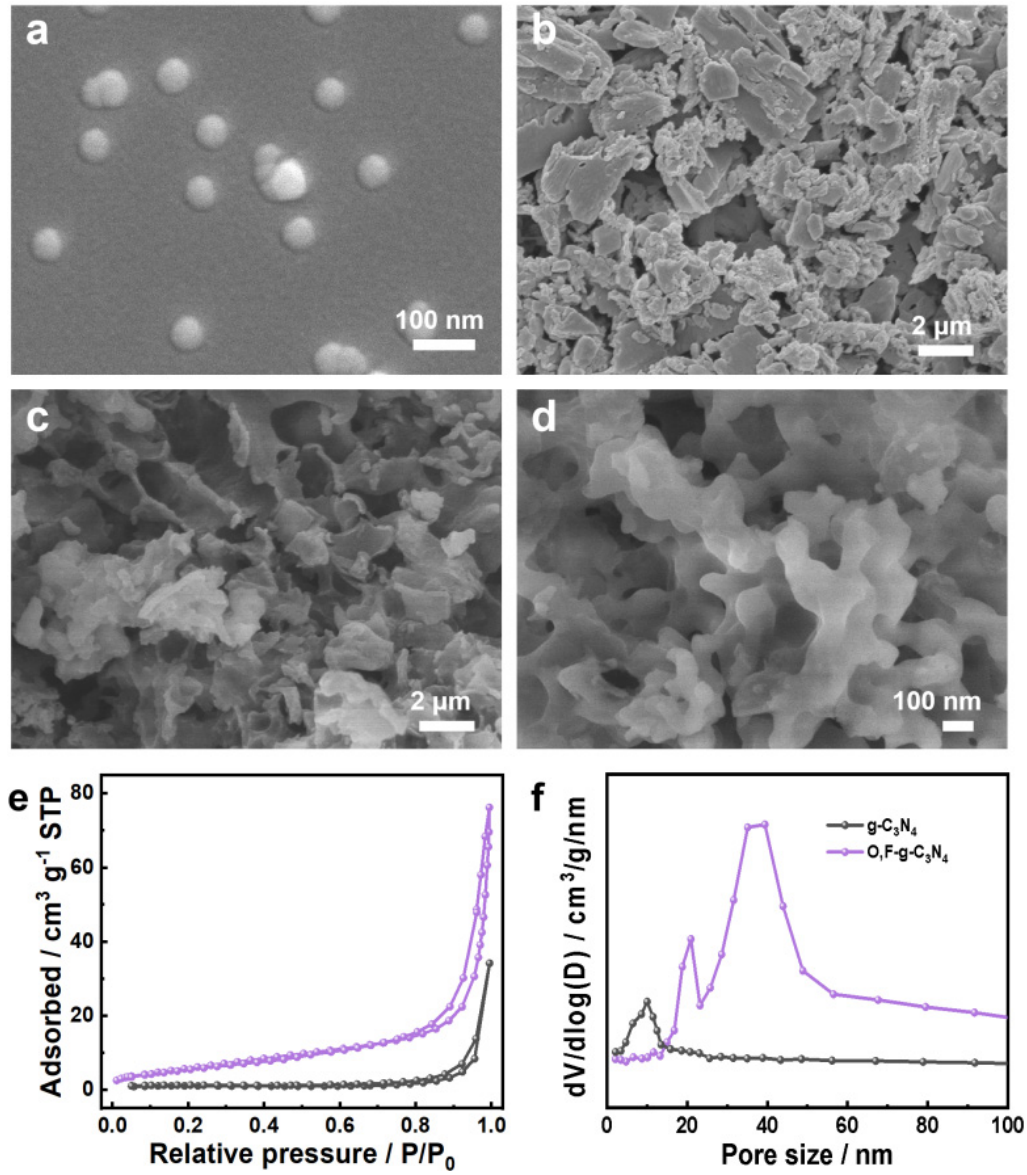



**Figure 1.** (**a**–**d**) SEM images of (**a**) colloidal $SiO_2$, (**b**) pristine g-$C_3N_4$ and (**c**,**d**) O,F-g-$C_3N_4$ photocatalyst. (**e**) Nitrogen adsorption–desorption isotherms and (**f**) corresponding pore size distribution curves of g-$C_3N_4$ and O,F-g-$C_3N_4$ photocatalysts.

Figure 2b presents the XRD patterns of the colloidal $SiO_2$, pristine g-$C_3N_4$ and O,F-g-$C_3N_4$ samples. The XRD pattern of colloidal $SiO_2$ showed a broad peak at 22.0°, a typical feature of amorphous silica [13]. In the XRD pattern of g-$C_3N_4$, two characteristic diffraction peaks appeared at 13.1° and 27.4°, corresponding to the (100) and (002) crystal planes, which were attributed to the repeating heptazine units and the layered, stacked conjugated aromatic structure (JCPDS 87-1526) [31]. The O,F-g-$C_3N_4$ sample displayed the characteristic peaks of g-$C_3N_4$ but with reduced peak intensity, indicating decreased crystallinity following $NH_4 \cdot HF_2$ treatment.

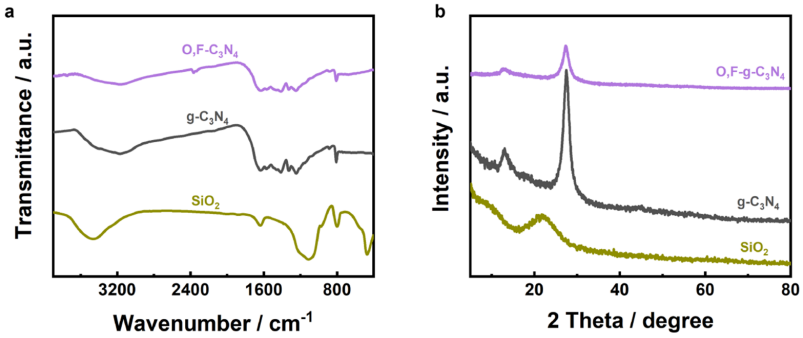



**Figure 2.** (**a**) FTIR spectra and (**b**) XRD patterns of the colloidal $SiO_2$, pristine g-$C_3N_4$ and O,F-g-$C_3N_4$ samples.

XPS measurements were conducted to determine the elemental valence states in the O,F-g-$C_3N_4$ photocatalyst (Figure 3). The survey XPS spectra confirmed the presence of C, N, O, Si and F elements (Figure S1). In the C 1s spectrum, peaks at 284.8 eV and 287.8 eV were attributed to the C–C and C–N=C groups, respectively (Figure 3a) [32]. Additionally, peaks at 286.1 eV and 289.0 eV corresponded to C–O and C–F bonds, respectively [32,33]. The high-resolution N 1s spectrum was deconvoluted in three peaks corresponding to the N–C=N, N–$(C)_3$, and $NH_x$ groups (Figure 3b) [34]. Besides the signal for adsorbed $H_2O$ at 532.7 eV, the O 1s peak at 530.8 eV was assigned to the C–O bond (Figure 3c) [32,35]. The F 1s peak at 688.4 eV corresponded to the C–F bond, achieved through $NH_4{\cdot}HF_2$ post-treatment (Figure 3d) [35]. Collectively, the FTIR, XRD and XPS analyses confirmed that the use of colloidal $SiO_2$ and $NH_4{\cdot}HF_2$ post-treatment successfully incorporated O and F into the g-$C_3N_4$ framework through chemical bonding, without altering the fundamental heptazine structure. The formed C–O bonds may serve as active sites for $H_2$ production, while fluorine incorporation facilitates electron transfer due to its high electronegativity. These modifications were beneficial for photocatalytic activity enhancement.

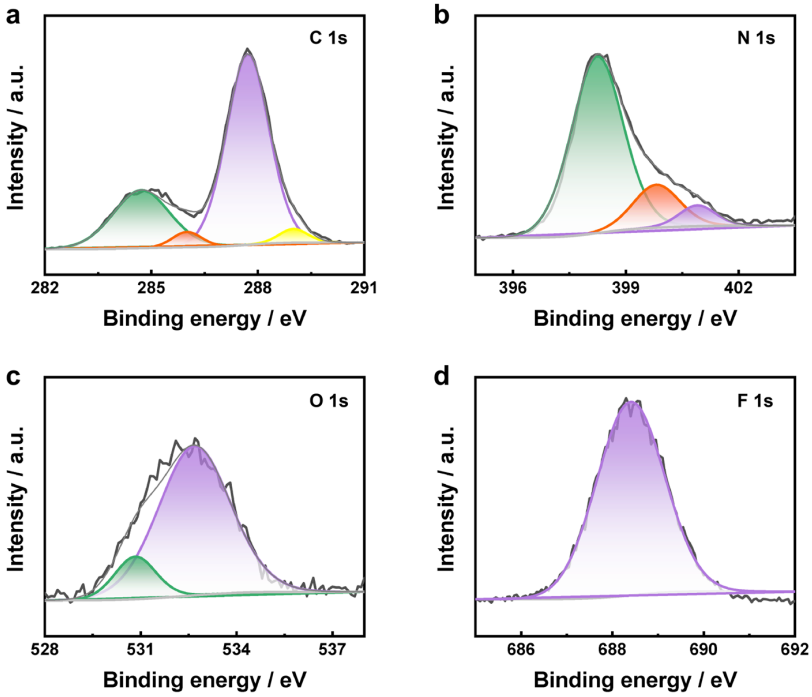



**Figure 3.** High-resolution XPS spectra of O,F-g-$C_3N_4$ sample: (**a**) C 1s, (**b**) N 1s, (**c**) O 1s and (**d**) F 1s.

### *3.2. Light Response and Photoelectric Conversion Efficiency Characterization*

The visible light response capacity of pristine g-$C_3N_4$ and O,F-g-$C_3N_4$ photocatalysts was assessed using UV-vis diffuse reflectance spectroscopy. Compared to bare g-$C_3N_4$, O,F-

g-$C_3N_4$ exhibited a red-shifted absorption edge and enhanced light absorption intensity (Figure 4a). Tauc plots indicate that the introduction of O and F narrowed the band gap, thereby extending the visible light absorption capacity of the O,F-g-$C_3N_4$ sample (Figure 4b).

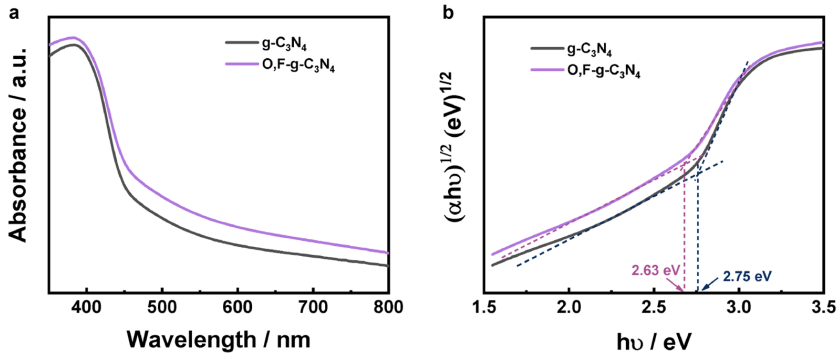



**Figure 4.** (**a**) UV-vis diffusion reflectance spectra and (**b**) Tauc plots of pristine g-$C_3N_4$ and O,F-g-$C_3N_4$ samples.

The photoelectric conversion efficiency of pristine g-$C_3N_4$ and O,F-g-$C_3N_4$ photocatalysts was evaluated using steady-state photoluminescence (PL) emission spectra, transient PL decay spectra, electrochemical impedance spectroscopy (EIS), and transient photocurrent responses (Figure 5). The effect of incorporated O and F on photoexcited charge carrier separation was assessed based on the peak intensity of the steady-state PL emission spectrum, where a lower PL intensity generally indicates the reduced recombination of photo-generated charge carriers [36]. As shown in Figure 5a, the O,F-g-$C_3N_4$ exhibited lower PL intensity compared to bare g-$C_3N_4$, indicating the promotion of the separation of photo-generated electron–hole pairs following O and F incorporation. The transient PL decay spectra further elucidated electron–hole pair dissociation kinetics [37]. Compared to pristine g-$C_3N_4$, the O,F-g-$C_3N_4$ photocatalyst exhibited a shorter exciton lifetime, suggesting faster dissociation dynamics of photoexcited charge carriers (Figure 5b).

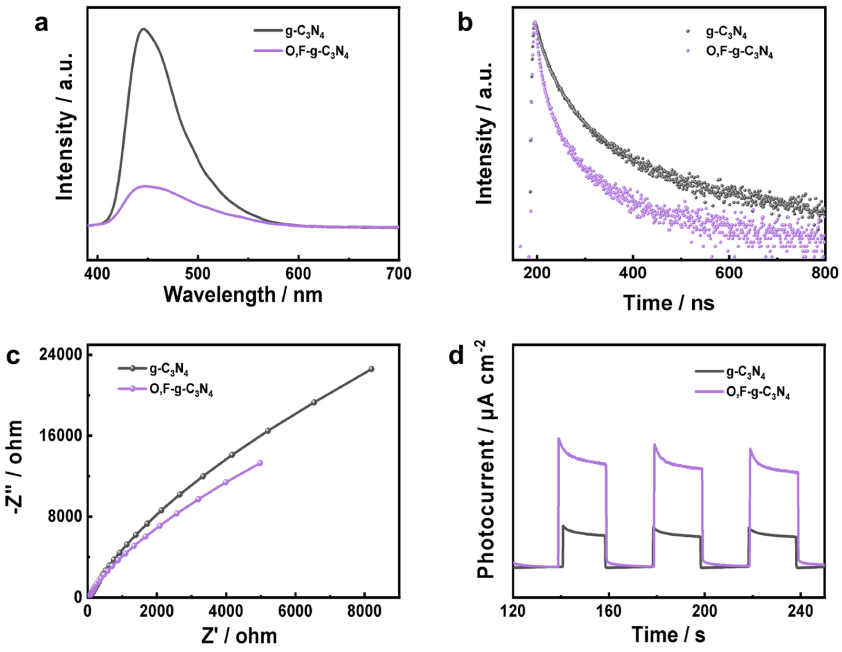



**Figure 5.** (**a**) PL emission spectra, (**b**) time−resolved PL decay curves, (**c**) EIS spectra and (**d**) periodic on/off photocurrent responses of bare g-$C_3N_4$ and O,F-g-$C_3N_4$ photocatalysts.

The migration efficiency of photo-induced charge carriers was assessed using the EIS spectra and transient photocurrent responses of the prepared photocatalysts. Notably, the Nyquist plot for the O,F-g-$C_3N_4$ sample exhibited a smaller slope than that of bare g-$C_3N_4$ (Figure 5c), indicating reduced charge transfer resistance to surface active sites [38]. Additionally, the significantly increased photocurrent density of O,F-g-$C_3N_4$ confirmed the improved transport efficiency of charge carriers (Figure 5d). These findings from light response and photoelectric conversion characterizations suggest that the O,F co-modification strategy provides a synergistic enhancement in light absorption and photoelectric conversion, thereby favoring improved photocatalytic performance.

### *3.3. Photocatalytic Performance Evaluation*

The photocatalytic $H_2$ evolution rates of the pristine g-$C_3N_4$ and O,F-g-$C_3N_4$ samples are shown in Figure 6a. Bare colloidal $SiO_2$ showed no photocatalytic hydrogen production activity. Pristine g-$C_3N_4$ exhibited a low $H_2$ production rate of 71.8 μmol·$h^{-1}$·$g^{-1}$. In contrast, the O,F-g-$C_3N_4$ sample demonstrated a significantly increased photocatalytic $H_2$ production rate (947.2 μmol·$h^{-1}$·$g^{-1}$), which was 13.2 times higher than that of bare g-$C_3N_4$. This suggests that O,F dual-element co-modification effectively enhanced the photocatalytic $H_2$ production performance of g-$C_3N_4$. The improved activity was attributed to the C–O and C–F bonds that formed after the introduction of O and F, which narrowed the electronic band gap and extended the visible light response. This co-modification also facilitated the separation and transport of photo-generated charge carriers. Meanwhile, the as-synthesized O,F-g-$C_3N_4$ sample also maintained its photocatalytic activity after four cycles of $H_2$ evolution tests (Figure 6b), confirming its excellent photo-stability for long-term reactions.

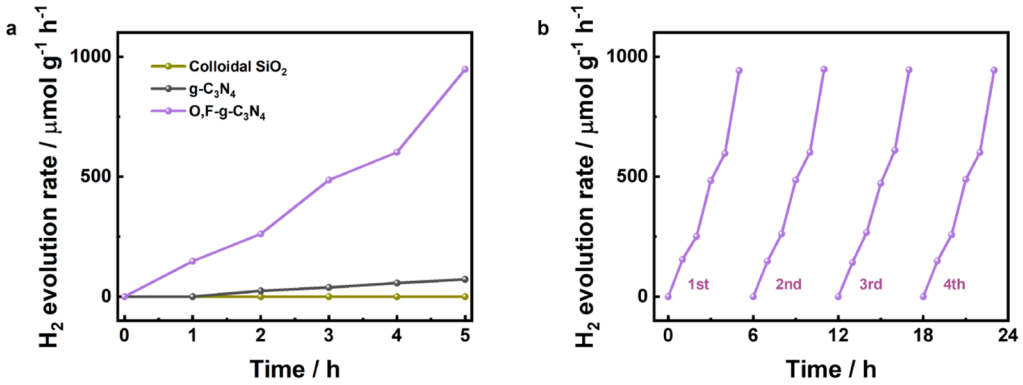



**Figure 6.** (**a**) The photocatalytic $H_2$ evolution rates of the colloidal $SiO_2$, pristine g-$C_3N_4$ and O,F-g-$C_3N_4$ samples. (**b**) The cyclic $H_2$ evolution tests of the O,F-g-$C_3N_4$ photocatalyst.

### *3.4. Anti-Corrosion Performance*

Water absorption rate is a common indicator of a coating's water resistance, with lower rates indicating stronger resistance. The water absorption rates of the pure WPU, g-$C_3N_4$@WPU composite coating and O,F-g-$C_3N_4$@WPU composite coating are shown in Figure 7a. The pure WPU coating exhibited the highest water absorption rate, reaching 6.27% after 36 h of immersion. Upon modification with g-$C_3N_4$, the water absorption rate of the g-$C_3N_4$@WPU composite coating decreased to 5.53%. Notably, the O,F-g-$C_3N_4$@WPU composite coating had the lowest water absorption rate of 4.51%. These lower water absorption rates of the composite coatings compared to pure WPU reveal that g-$C_3N_4$ enhances the water resistance of WPU, with optimal resistance achieved by O and F dual-element doping. This improvement is likely attributed to the introduction of lamellar photocatalysts, which act as a barrier against water intrusion.

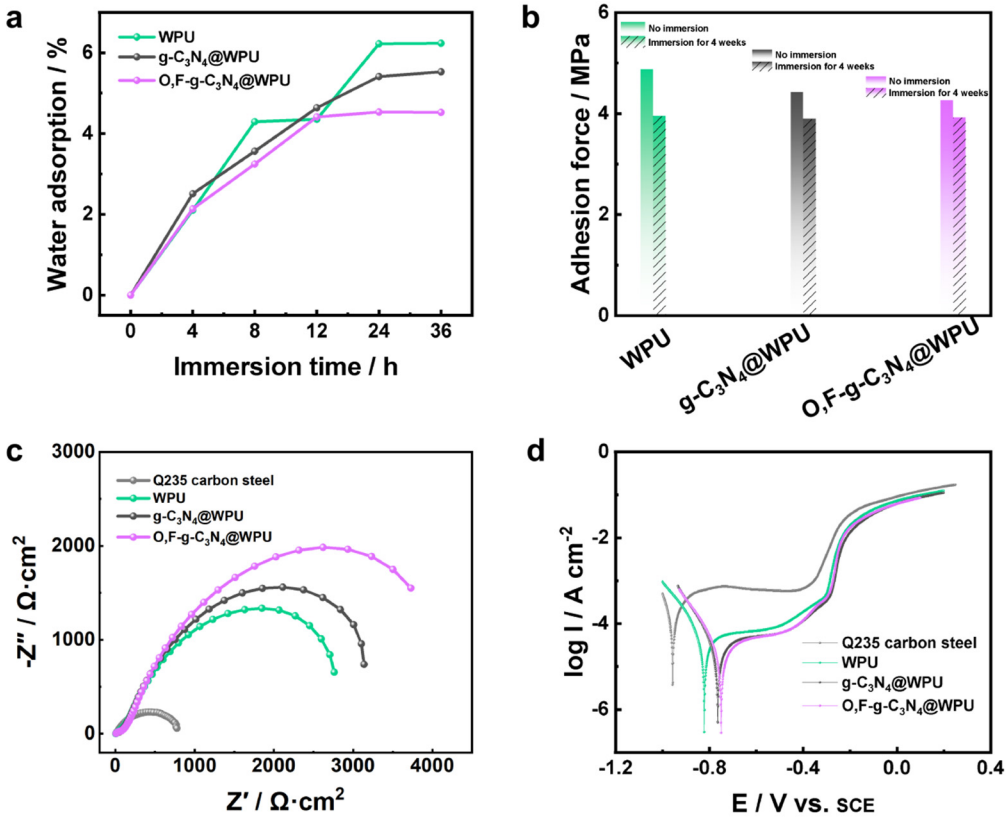



**Figure 7.** (**a**) Water absorption and (**b**) adhesion force of pure WPU, g-$C_3N_4$@WPU and O,F-g-$C_3N_4$@WPU coatings. (**c**) EIS spectra and (**d**) Tafel curves of Q235 carbon steel, pure WPU, g-$C_3N_4$@WPU and O,F-g-$C_3N_4$@WPU coatings in NaCl aqueous solution (3.5 wt.%).

The adhesion strength between the coating and substrate is another metric for measuring the barrier properties of the coating. Adhesion was tested after immersion in a 3.5 wt.% NaCl solution for 4 weeks, and the results are shown in Figure 7b. Initially, the adhesion strengths of the pure WPU, g-$C_3N_4$@WPU and O,F-g-$C_3N_4$@WPU coatings were 4.87, 4.41 and 4.26 MPa, respectively. After immersion, these values decreased to 3.95, 3.89 and 3.92 MPa, respectively. The pure WPU coating showed the highest adhesion loss rate (18.89%) after immersion, whereas the g-$C_3N_4$@WPU and O,F-g-$C_3N_4$@WPU composite coatings exhibited significantly lower adhesion loss rates. The O,F-g-$C_3N_4$@WPU composite coating had the smallest adhesion loss rate of 7.45%, representing only 39.44% of the loss rate observed in pure WPU. These results indicate that the addition of O,F-g-$C_3N_4$ enhances the barrier properties of the WPU coating, effectively preventing the penetration of corrosive media into the substrate and thereby mitigating separation between the coating and the Q235 substrate surface.

The barrier properties and corrosion resistance of the coating on the surface of Q235 carbon steel were assessed using EIS spectra and polarization curves. Nyquist plots and Tafel curves were acquired by immersing the prepared coatings in a NaCl solution (3.5 wt.%) for 4 weeks, mimicking a corrosive environment. Figure 7c shows the Nyquist plots of different coatings, whose larger arc diameter implies better protective performance. It was obviously observed that both the g-$C_3N_4$@WPU and O,F-g-$C_3N_4$@WPU coatings exhibited larger initial arc diameters than the bare WPU coating, signifying enhanced corrosion resistance due to the addition of a photocatalyst. A comparative analysis revealed that the O,F-g-$C_3N_4$@WPU coating outperformed the g-$C_3N_4$@WPU coating in terms of corrosion resistance, highlighting the advantages of co-modification with O and F. The Tafel curves showed an analogous trend (Figure 7d). It is well known that corrosion potential ($E_{corr}$) and protection efficiency (η) obtained from Tafel curves can reflect the corrosion resistance

of coatings, that is, a more positive corrosion potential indicates better the anti-corrosion performance. By analyzing the changes in the $E_{corr}$ values of the pure WPU coating and coatings containing g-$C_3N_4$ and O,F-g-$C_3N_4$, the corrosion inhibition mechanism can be elucidated. According to the literature [39], if the change in $E_{corr}$ exceeds 85 mV, the inhibition mechanism is classified as either anodic or cathodic. Changes below 85 mV indicate a mixed inhibition mechanism involving both anodic and cathodic processes. The differences in $E_{corr}$ values between the g-$C_3N_4$@WPU coating and the blank sample, as well as between the O,F-g-$C_3N_4$@WPU coating and the blank sample, were 75.9 mV and 65.9 mV, respectively (Table S2). These results indicate that both coatings exhibit a mixed inhibition mechanism. Furthermore, the O,F-g-$C_3N_4$@WPU coating demonstrated the highest protection efficiency (90.23%) compared to the blank sample, providing additional evidence of its superior ability to mitigate the corrosion of Q235 carbon steel.

## 4. Conclusions

In summary, we successfully synthesized an O and F co-modified g-$C_3N_4$ photocatalyst using colloidal $SiO_2$ as the O source and $NH_4{\cdot}HF_2$ as the F source. A mechanism was proposed to explain the enhanced photocatalytic $H_2$ production and anti-corrosion performance of O,F-g-$C_3N_4$. The introduction of O and F formed C–O and C–F bonds, which narrowed the electronic band gap and extended the visible light response. This co-modification also facilitated the separation and transport of photo-generated charge carriers. The synthesized O,F-g-$C_3N_4$ photocatalyst exhibited both improved photocatalytic $H_2$ production activity and enhanced corrosion resistance. When uniformly dispersed within the WPU matrix, the increased surface area and barrier effect of O,F-g-$C_3N_4$ provided effective corrosion protection for Q235 carbon steel.

**Supplementary Materials:** The following supporting information can be downloaded at: https://www.mdpi.com/article/10.3390/cryst14121063/s1, Figure S1: Survey XPS spectra of O,F-$C_3N_4$ sample; Table S1: Textural properties of pristine g-$C_3N_4$ and O,F-$C_3N_4$ samples; Table S2: Potentiodynamic polarization parameters of different coatings before and after four weeks of immersion in 3.5 wt.% NaCl.

**Author Contributions:** S.Z.: Writing—Original Draft, Visualization, Investigation, Data Curation. P.L.: Visualization, Validation, Supervision. C.Z.: Investigation. Y.W.: Investigation, Data Curation. J.H.: Investigation. R.J.: Investigation, Writing—Review and Editing. All authors have read and agreed to the published version of the manuscript.

**Funding:** This research was funded by the Jilin Electric Power Science Research Institute Co., Ltd., Science and Technology Development Project (KY-GS-24-01-05).

**Data Availability Statement:** The data presented in this study are available on request from the corresponding author.

**Conflicts of Interest:** The authors declare no conflicts of interest.

## References

1. Barrio, J.; Volokh, M.; Shalom, M. Polymeric carbon nitrides and related metal-free materials for energy and environmental applications. *J. Mater. Chem. A* **2020**, *8*, 11075–11116. [CrossRef]
2. Wang, S.; Zhu, B.; Liu, M.; Zhang, L.; Yu, J.; Zhou, M. Direct Z-scheme ZnO/CdS hierarchical photocatalyst for enhanced photocatalytic $H_2$-production activity. *Appl. Catal. B Environ.* **2019**, *243*, 19–26. [CrossRef]
3. Sarfaraz, S.; Yar, M.; Ashraf, M.U.; Ayub, K. Highly efficient transition metal doped C24 electrocatalysts for hydrogen evolution reaction: Kinetic and thermodynamic aspects. *Mat. Sci. Semicon Proc.* **2023**, *168*, 107840. [CrossRef]
4. Liang, H.; Mei, J.; Sun, H.; Cao, L. Enhanced photocatalytic hydrogen evolution of CdS@CuS core-shell nanorods under visible light. *Mat. Sci. Semicon Proc.* **2023**, *153*, 107105. [CrossRef]
5. Yang, C.; Xue, Z.; Qin, J.; Sawangphruk, M.; Rajendran, S.; Zhang, X.; Liu, R. Visible light-driven photocatalytic $H_2$ generation and mechanism insights into $Bi_2O_2CO_3$/g-$C_3N_4$ Z-scheme photocatalyst. *J. Phys. Chem. C* **2019**, *123*, 4795–4804. [CrossRef]
6. You, Y.; Wang, S.; Xiao, K.; Ma, T.; Zhang, Y.; Huang, H. Z-Scheme g-$C_3N_4$/$Bi_4NbO_8Cl$ heterojunction for enhanced photocatalytic hydrogen production. *ACS Sustain. Chem. Eng.* **2018**, *6*, 16219–16227. [CrossRef]

7. Fan, X.; Zhang, L.; Wang, M.; Huang, W.; Zhou, Y.; Li, M.; Cheng, R.; Shi, J. Constructing carbon-nitride-based copolymers via Schiff base chemistry for visible-light photocatalytic hydrogen evolution. *Appl. Catal. B Environ.* **2016**, *182*, 68–73. [CrossRef]
8. Che, W.; Cheng, W.; Yao, T.; Tang, F.; Liu, W.; Su, H.; Huang, Y.; Liu, Q.; Liu, J.; Hu, F. Fast photoelectron transfer in (Cring)–$C_3N_4$ plane heterostructural nanosheets for overall water splitting. *J. Am. Chem. Soc.* **2017**, *139*, 3021–3026. [CrossRef]
9. Wang, Y.; Liu, X.; Liu, J.; Han, B.; Hu, X.; Yang, F.; Xu, Z.; Li, Y.; Jia, S.; Li, Z.; et al. Carbon quantum dot implanted graphite carbon nitride nanotubes: Excellent charge separation and enhanced photocatalytic hydrogen evolution. *Angew. Chem. Int. Ed.* **2018**, *130*, 5867–5873. [CrossRef]
10. Li, J.; Wu, D.; Iocozzia, J.; Du, H.; Liu, X.; Yuan, Y.; Zhou, W.; Li, Z.; Xue, Z.; Lin, Z. Achieving efficient incorporation of Π-electrons into graphitic carbon nitride for markedly improved hydrogen generation. *Angew. Chem. Int. Ed.* **2019**, *131*, 2007–2011. [CrossRef]
11. Li, Y.; Wang, Z.; Xia, T.; Ju, H.; Zhang, K.; Long, R.; Xu, Q.; Wang, C.; Song, L.; Zhu, J. Implementing metal-to-ligand charge transfer in organic semiconductor for improved visible-near-infrared photocatalysis. *Adv. Mater.* **2016**, *28*, 6959–6965. [CrossRef] [PubMed]
12. Wang, Y.; Wang, X.; Antonietti, M.; Zhang, Y. Facile one-pot synthesis of nanoporous carbon nitride solids by using soft templates. *ChemSusChem* **2010**, *3*, 435–439. [CrossRef] [PubMed]
13. Jia, R.; Yu, X.; Yang, X.; Wang, X.; Yang, J.; Huo, X.; Qi, Q. Porous graphitic carbon nitride with high concentration of oxygen promotes photocatalytic $H_2$ evolution. *RSC Adv.* **2022**, *12*, 33688–33695. [CrossRef] [PubMed]
14. Su, F.; Mathew, S.C.; Lipner, G.; Fu, X.; Antonietti, M.; Blechert, S.; Wang, X. mpg-$C_3N_4$-catalyzed selective oxidation of alcohols using $O_2$ and visible light. *J. Am. Chem. Soc.* **2010**, *132*, 16299–16301. [CrossRef]
15. Sun, J.; Zhang, J.; Zhang, M.; Antonietti, M.; Fu, X.; Wang, X. Bioinspired hollow semiconductor nanospheres as photosynthetic nanoparticles. *Nat. Commun.* **2012**, *3*, 1139. [CrossRef]
16. Yang, X.; Wang, X.; Yang, J.; Bian, X.; Yu, X.; Huo, X.; Qia, Q.; Jia, R. The synthesis of porous graphitic carbon nitride with $N_{3C}$ nitrogen vacancies by a $CaCO_3$ template for improved photocatalytic $H_2$ evolution. *New J. Chem.* **2022**, *46*, 13783–13790. [CrossRef]
17. Zhang, H.; Bao, C.; Hu, X.; Wen, Y.; Li, K.; Zhang, H. Synthesis of tunnel structured g-$C_3N_4$ through a facile vapor deposition method using SBA-15 and KIT-6 as templates and their photocatalytic degradation of tetracycline hydrochloride and phenol. *J. Environ. Chem. Eng.* **2022**, *10*, 107871. [CrossRef]
18. Bai, X.; Li, H.; Zhang, Z.; Zhang, X.; Wang, C.; Xu, J.; Zhu, Y. Carbon nitride nested tubes with graphene as a dual electron mediator in Z-scheme photocatalytic deoxynivalenol degradation. *Catal. Sci. Technol.* **2019**, *9*, 1680–1690. [CrossRef]
19. Yang, P.; Zhuzhang, H.; Wang, R.; Lin, W.; Wang, X. Carbon vacancies in a melon polymeric matrix promote photocatalytic carbon dioxide conversion. *Angew. Chem. Int. Ed.* **2019**, *58*, 1134–1137. [CrossRef]
20. Moon, G.-h.; Fujitsuka, M.; Kim, S.; Majima, T.; Wang, X.; Choi, W. Eco-friendly photochemical production of $H_2O_2$ through $O_2$ reduction over carbon nitride frameworks incorporated with multiple heteroelements. *ACS Catal.* **2017**, *7*, 2886–2895. [CrossRef]
21. Lan, Z.-A.; Zhang, G.; Wang, X. A facile synthesis of Br-modified g-$C_3N_4$ semiconductors for photoredox water splitting. *Appl. Catal. B Environ.* **2016**, *192*, 116–125. [CrossRef]
22. Wang, Y.; Di, Y.; Antonietti, M.; Li, H.; Chen, X.; Wang, X. Excellent visible-light photocatalysis of fluorinated polymeric carbon nitride solids. *Chem. Mater.* **2010**, *22*, 5119–5121. [CrossRef]
23. Zhang, G.; Zhang, M.; Ye, X.; Qiu, X.; Lin, S.; Wang, X. Iodine modified carbon nitride semiconductors as visible light photocatalysts for hydrogen evolution. *Adv. Mater.* **2013**, *26*, 805–809. [CrossRef] [PubMed]
24. Gao, Y.; Zhu, Y.; Lyu, L.; Zeng, Q.; Xing, X.; Hu, C. Electronic structure modulation of graphitic carbon nitride by oxygen doping for enhanced catalytic degradation of organic pollutants through peroxymonosulfate activation. *Environ. Sci. Technol.* **2018**, *52*, 14371–14380. [CrossRef]
25. Li, L.; Shi, Y.; Xu, Z.; Sun, H.; Amin, S.; Yang, X.; Guo, F.; Shi, W. Environmentally friendly synthesis of oxygen-doped g-$C_3N_4$ nanosheets for enhancing photocatalytic corrosion resistance of carbon steel. *Prog. Org. Coat.* **2022**, *163*, 106628. [CrossRef]
26. Zhang, S.; Shen, Y.; Lu, J.; Chen, Z.; Li, L.; Guo, F.; Shi, W. Tannic acid-modified g-$C_3N_4$ nanosheets/polydimethylsiloxane as a photothermal-responsive self-healing composite coating for smart corrosion protection. *Chem. Eng. J.* **2024**, *483*, 149232. [CrossRef]
27. Samadianfard, R.; Seifzadeh, D.; Dikici, B. Smart sol-gel nanocomposite containing inhibitor-stabilized g-$C_3N_4$ nanoplates for corrosion protection of magnesium alloy. *Surf. Coat. Tech.* **2024**, *484*, 130764. [CrossRef]
28. Hasanzadeh, A.; SaadatAbadi, A.R. ZIF-67 metal-organic framework decorated g-$C_3N_4$ nanosheets with inbuilt organic-inorganic corrosion inhibitor for self-healing epoxy anti-corrosion coating. *Surf. Coat. Tech.* **2024**, *492*, 131218. [CrossRef]
29. Han, Y.; Guo, Z.; Teng, S.; Xia, H.; Wang, D.; Han, M.-Y.; Yang, W. Rationalized fabrication of structure-tailored multishelled hollow silica spheres. *Chem. Mater.* **2019**, *31*, 7470–7477. [CrossRef]
30. Navarchian, A.H.; Joulazadeh, M.; Karimi, F. Investigation of corrosion protection performance of epoxy coatings modified by polyaniline/clay nanocomposites on steel surfaces. *Prog. Org. Coat.* **2014**, *77*, 347–353. [CrossRef]
31. Qin, Y.; Li, H.; Lu, J.; Feng, Y.; Meng, F.; Ma, C.; Yan, Y.; Meng, M. Synergy between van der waals heterojunction and vacancy in $ZnIn_2S_4$/g-$C_3N_4$ 2D/2D photocatalysts for enhanced photocatalytic hydrogen evolution. *Appl. Catal. B Environ.* **2020**, *277*, 119254. [CrossRef]
32. Yang, X.; Bian, X.; Yu, W.; Wang, Q.; Huo, X.; Teng, S. Organosilica-assisted superhydrophilic oxygen doped graphitic carbon nitride for improved photocatalytic $H_2$ evolution. *Int. J. Hydrogen Energy* **2022**, *47*, 34444–34454. [CrossRef]

33. Chen, Z.; Chen, W.; Liao, G.; Li, X.; Wang, J.; Tang, Y.; Li, L. Flexible construct of N vacancies and hydrophobic sites on g-$C_3N_4$ by F doping and their contribution to PFOA degradation in photocatalytic ozonation. *J. Hazard. Mater.* **2022**, *428*, 128222. [CrossRef] [PubMed]
34. Cheng, J.; Hou, Y.; Lian, K.; Xiao, H.; Lin, S.; Wang, X. Metalized carbon nitrides for efficient catalytic functionalization of $CO_2$. *ACS Catal.* **2022**, *12*, 1797–1808. [CrossRef]
35. Yang, C.; Yang, J.; Liu, S.; Zhao, M.; Duan, X.; Wu, H.; Liu, L.; Liu, W.; Li, J.; Ren, S.; et al. Constructing C–O bridged $CeO_2$/g-$C_3N_4$ S-scheme heterojunction for methyl orange photodegradation: Experimental and theoretical calculation. *J. Environ. Manag.* **2023**, *335*, 117608. [CrossRef]
36. Simbula, A.; Wu, L.; Pitzalis, F.; Pau, R.; Lai, S.; Liu, F.; Matta, S.; Marongiu, D.; Quochi, F.; Saba, M.; et al. Exciton dissociation in 2D layered metal-halide perovskites. *Nat. Commun.* **2023**, *14*, 4125. [CrossRef]
37. Lu, Y.; Liu, Y.-X.; He, L.; Wang, L.-Y.; Liu, X.-L.; Liu, J.-W.; Li, Y.-Z.; Tian, G.; Zhao, H.; Yang, X.-H.; et al. Interfacial co-existence of oxygen and titanium vacancies in nanostructured $TiO_2$ for enhancement of carrier transport. *Nanoscale* **2020**, *12*, 8364–8370. [CrossRef]
38. Hung, S.; Xiao, F.; Hsu, Y.; Suen, N.; Yang, H.; Chen, H.M.; Liu, B. Iridium oxide assisted plasmon induced hot carriers: Improvement on kinetics and thermodynamics of hot carriers. *Adv. Energy Mater.* **2016**, *6*, 1501339. [CrossRef]
39. Qiang, Y.; Zhang, S.; Tan, B.; Chen, S. Evaluation of Ginkgo leaf extract as an ecofriendly corrosion inhibitor of X70 steel in HCl solution. *Corros. Sci.* **2018**, *133*, 6–16. [CrossRef]


**Disclaimer/Publisher's Note:** The statements, opinions and data contained in all publications are solely those of the individual author(s) and contributor(s) and not of MDPI and/or the editor(s). MDPI and/or the editor(s) disclaim responsibility for any injury to people or property resulting from any ideas, methods, instructions or products referred to in the content.